Astronomy & Astrophysics manuscript no. ms-ngc7538_arxiv
May 24, 2019

Deuterated methanol toward NGC 7538-IRS1⋆

J. Ospina-Zamudio[1], C. Favre[1,2], M. Kounkel[3], L-H. Xu[4,⋆], J. Neill[5], B. Lefloch[1], A. Faure[1], E. Bergin[5], D. Fedele[2], and L. Hartmann[5]

[1] Univ. Grenoble Alpes, CNRS, IPAG, F-38000 Grenoble, France
e-mail: juan-david.ospina-zamudio@univ-grenoble-alpes.fr
[2] INAF-Osservatorio Astrofisico di Arcetri, Largo E. Fermi 5, I-50125, Florence, Italy
[3] Department of Physics and Astronomy, Western Washington University, 516 High St, Bellingham, WA 98225
[4] Centre for Laser, Atomic, and Molecular Sciences (CLAMS), Department of Physics, University of New Brunswick, PO Box 5050, Saint John, NB, Canada E2L 4L5
[5] Department of Astronomy, University of Michigan, 1085 South University Avenue, Ann Arbor, Michigan 48109, USA

May 24, 2019

ABSTRACT

We investigate the deuteration of methanol towards the high-mass star forming region NGC 7538-IRS1. We have carried out a multi-transition study of CH_3OH, $^{13}CH_3OH$ and of the deuterated flavors, CH_2DOH and CH_3OD, between 1.0–1.4 mm with the IRAM-30 m antenna. In total, 34 $^{13}CH_3OH$, 13 CH_2DOH lines and 20 CH_3OD lines spanning a wide range of upper-state energies (E_{up}) were detected. From the detected transitions, we estimate that the measured D/H does not exceed 1%, with a measured CH_2DOH/CH_3OH and CH_3OD/CH_3OH of about $(32\pm8)\times10^{-4}$ and $(10\pm4)\times10^{-4}$, respectively. This finding is consistent with the hypothesis of a short-time scale formation during the pre-stellar phase. We find a relative abundance ratio CH_2DOH/CH_3OD of 3.2 ± 1.5. This result is consistent with a statistical deuteration. We cannot exclude H/D exchanges between water and methanol if water deuteration is of the order 0.1%, as suggested by recent Herschel observations.

Key words. ISM: molecules – ISM: abundance – Radio lines: ISM

1. Introduction

Observational studies of deuterated molecules are powerful ways to probe the chemical and physical evolution of star-forming regions. Indeed, many of the organic species that are abundant constituents of molecular clouds are synthesized in the cold prestellar phase (see Caselli & Ceccarelli 2012, for a review). At low temperatures, the difference in zero-point energy between deuterated molecules and their hydrogenated counterparts (about 1000 K for methanol and its singly deuterated flavors, Nandi et al. 2018) makes it possible for deuterated species to be formed with significantly higher relative abundances than the elemental D/H ratio ($\sim10^{-5}$, see e.g. Ceccarelli et al. 2007; Caselli & Ceccarelli 2012; Ceccarelli et al. 2014). These enhanced abundance ratios can be preserved as the protostar heats the gas to temperatures large enough (≥100 K) to evaporate the ice mantles. Thus, studies of molecular D/H ratios can provide strong insight into the physical history of star-forming regions along with information on the chemical routes through which the molecular content is formed. Deuterium fractionation in low-mass star-forming regions has been the subject of significant study (e.g., see Roberts et al. 2002; Parise et al. 2006; Ratajczak et al. 2011; Jørgensen et al. 2018). These sources have shown remarkably high enhancements of deuterated molecules, including even doubly and triply deuterated species (e.g. ND_3, CD_3OH), which, in some cases, occur at abundances 12-13 orders of magnitude higher than elemental abundance would suggest (Lis et al. 2002; Parise et al. 2002, 2004). Regarding high-mass star forming regions, only a few observations of deuterated molecules have been performed so far (e.g. Jacq et al. 1993; Ratajczak et al. 2011; Peng et al. 2012; Neill et al. 2013b,a) the best studied high-mass source of deuterated molecules being the Orion KL nebula. Low levels of fractionation are typically observed, consistent with molecular formation at higher temperatures; alternatively, warm gas-phase chemistry could alter the D/H ratio in high-mass regions during the post-evaporative phase. Interestingly enough, from chemical modelling using experimental kinetic data, Faure et al. (2015a) suggested that the D/H ratio measured in Orion-KL might not be representative of the original mantles due to deuterium exchanges between water and methanol in interstellar ices during the warm up phase. The study of the abundance ratio of the deuterated isotopologues methanol (CH_3OD/CH_2DOH) could give access to the initial deuteration of water ices before the warm up phase sets in. Nonetheless, taking into account the limited number of observations of deuterated species in high-mass star-forming regions, the extent to which the D/H ratios observed toward Orion KL are representative of high-mass sources chemistry is uncertain. Bøgelund et al. (2018) have recently reported low deuteration levels of methanol towards the HMSFR NGC6334 I, with typical values in the range of 0.01–1% for both CH_2DOH and CH_3OD. Large uncertainties on the column densities, of a factor of 4 to 10 depending on the species remain however, which prevent any robust conclusions on the CH_2DOH/CH_3OD ratio and the initial ice composition. Further observations of a sample of high-mass sources are thus required for comparison between sources and for improving our understanding of the chemistry that creates organic molecules with significant deuterium frac-

⋆ **This paper is dedicated to the memory of our dear colleague, Dr. Li-Hong Xu, who recently passed away.**

tionation (in particular, the roles of grain-surface and gas-phase reactions).

In this study, we investigate the D/H ratio for methanol (CH_3OH, CH_2DOH and CH_3OD) towards the high-mass forming region NGC 7538-IRS1 ($L = 1.3\times10^5\ L_\odot$, $d = 2.8$ kpc, $M \sim 30\ M_\odot$, see Bisschop et al. 2007; Beuther et al. 2012), which is known to harbour high abundances of organic molecules, including methanol (e.g Bisschop et al. 2007; Wirström et al. 2011). Results are given in Section 3 and discussed in Section 4.

2. Observations and data reduction

The data were acquired with the IRAM 30–m telescope on 2013 December 5, 6 and 10 towards NGC 7538-IRS1 with a single pointing (α_{J2000}=23^{h}13^{m}45^s.5, δ_{J2000}= +61°28′12″.0). The v_{LSR} was -57 km s^{-1}. The observations were taken in position switching mode, using a reference for the OFF position at [−600″, 0″]. The EMIR receiver at 1 mm was used in connection with the Fourier transform spectrometer (FTS) as backend, providing a spectral resolution 195 kHz. The spectral resolution was subsequently degraded to 780 KHz, which corresponds to about 1 km s^{-1}, in order to improve the signal-to-noise ratio of the data. The following frequency ranges were covered: 212.6–220.4 GHz, 228.3–236.0 GHz, 243.5–251.3 GHz, 251.5–259.3 GHz, 259.3–267.0 GHz and 267.2–274.9 GHz. The half-power beam sizes are 10″ and 12″ for observations at 250 GHz and 212 GHz, respectively.

The data were reduced using the CLASS90 package from the GILDAS software[1]. The spectra are reported in this study in main beam temperature units, T_{MB}, given by $T_{MB} = \frac{\eta_f}{\eta_{MB}} \times T_A^*$, where T_A^* is the antenna temperature, η_f the forward efficiency (η_f = 94, 92 and 87 at 210, 230 and 274 GHz, respectively) and η_{MB} the main beam efficiency (η_{MB}= 63, 59, 49 at 210, 230 and 274 GHz, respectively[2]). Finally, the data presented some spurs along with standing waves, which have been removed during the data reduction. In this paper, we focus on methanol and its deuterated flavors.

The spectroscopic parameters of the targeted lines are given in Appendix A (see Tables A.1 to A.4). More specifically, we used the spectroscopic data parameters[3] from Xu & Hougen (1995a,b), Xu & Lovas (1997), Xu et al. (2008) and Müller et al. (2004) for CH_3OH. The parameters for CH_2DOH come from Pearson et al. (2012) and that for $^{13}CH_3OH$ are from Xu & Lovas (1997); Xu et al. (1996, 2008, 2014). Regarding CH_3OD, we used the same unpublished data as Neill et al. (2013a) used for analysing the HIFI/Herschel observations of Orion-KL. Nonetheless, the CH_3OD partition functions we use in the present study (see also, Walsh et al. 2000) are given in Appendix B. Finally, collisional rates are assumed to be identical to those of CH_3OH and taken from Rabli & Flower (2010). This point is addressed in more detail in Section 3.3

3. Results and analysis

3.1. Detected Lines

We detect several bright lines covering a wide range of upper energy levels: 34 $^{13}CH_3OH$ lines with E_{up} spanning from 23 to 397 K; 13 CH_2DOH lines with E_{up} spanning from 25 to 94 K; and 20 CH_3OD lines (10 lines for both A- and E- forms) with E_{up} spanning from 19 to 271 K. The observational line parameters of the clearly detected transitions are summarised in Tables A.1 to A.4).

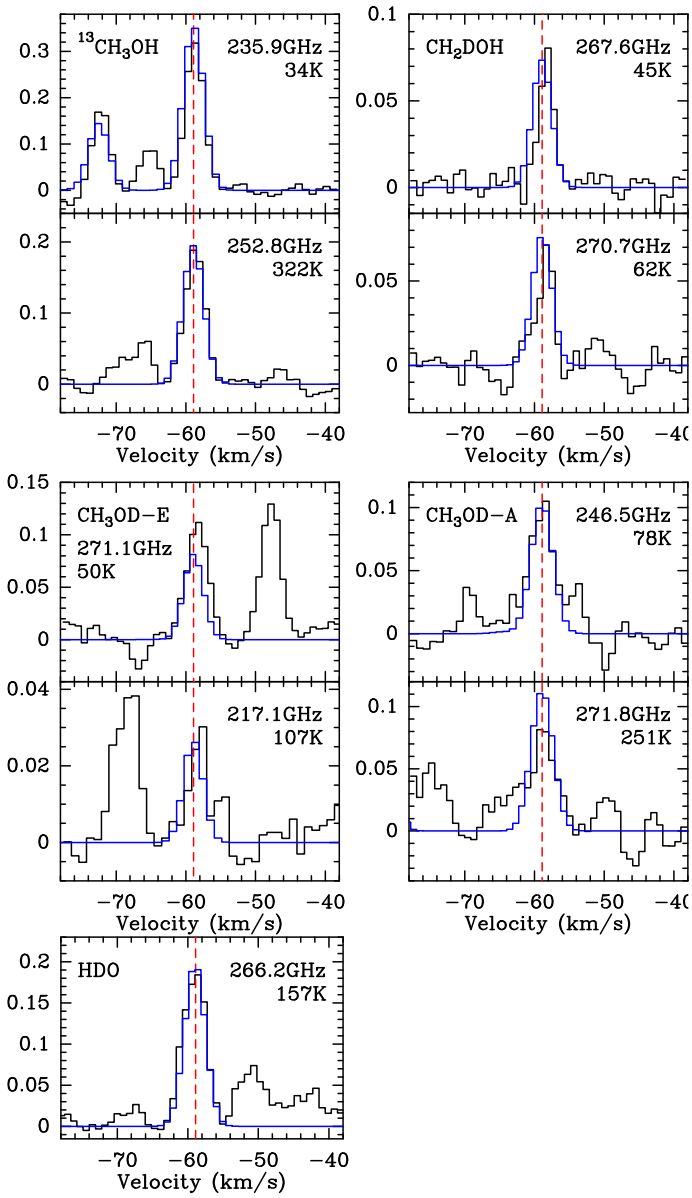

Fig. 1. Montage of detected transitions of methanol ^{13}C isotopologue and deuterated forms along with that of the detected HDO line. Intensities are expressed in unit of T_{mb}. Our LTE modelling is displayed in blue. The red dashed line marks the peak velocity of methanol transitions v_{LSR} = −58.9 km s^{-1}.

The lines profiles are well fitted by a single Gaussian profile with a little scatter on the fitted full-width half-maximum (mean $\Delta v = 3.4 \pm 0.7$ km s^{-1}) and the peak intensity velocity (mean $v_{LSR} = 58.6 \pm 0.6$ km s^{-1}). We note that the scatter on the peak velocity lies within 1 element of spectral resolution (1 km s^{-1}), which makes us confident with the line assignations. In addition, if we take into account the pointing uncertainties (typically 1″–2″), the observed scatter in emission velocity peak is consistent with the large velocity gradient observed within the source by Beuther et al. (2012, and their Fig. 8). Figure 1 show a montage of 2 detected transitions probing different excitation energies of

[1] http://www.iram.fr/IRAMFR/GILDAS/
[2] see http://www.iram.es/IRAMES/mainWiki/Iram30mEfficiencies
[3] The spectroscopic data parameters are available at the Cologne Database for Molecular Spectroscopy catalog (CDMS Müller et al. 2005) and/or at the JPL catalog (Pickett et al. 1998).

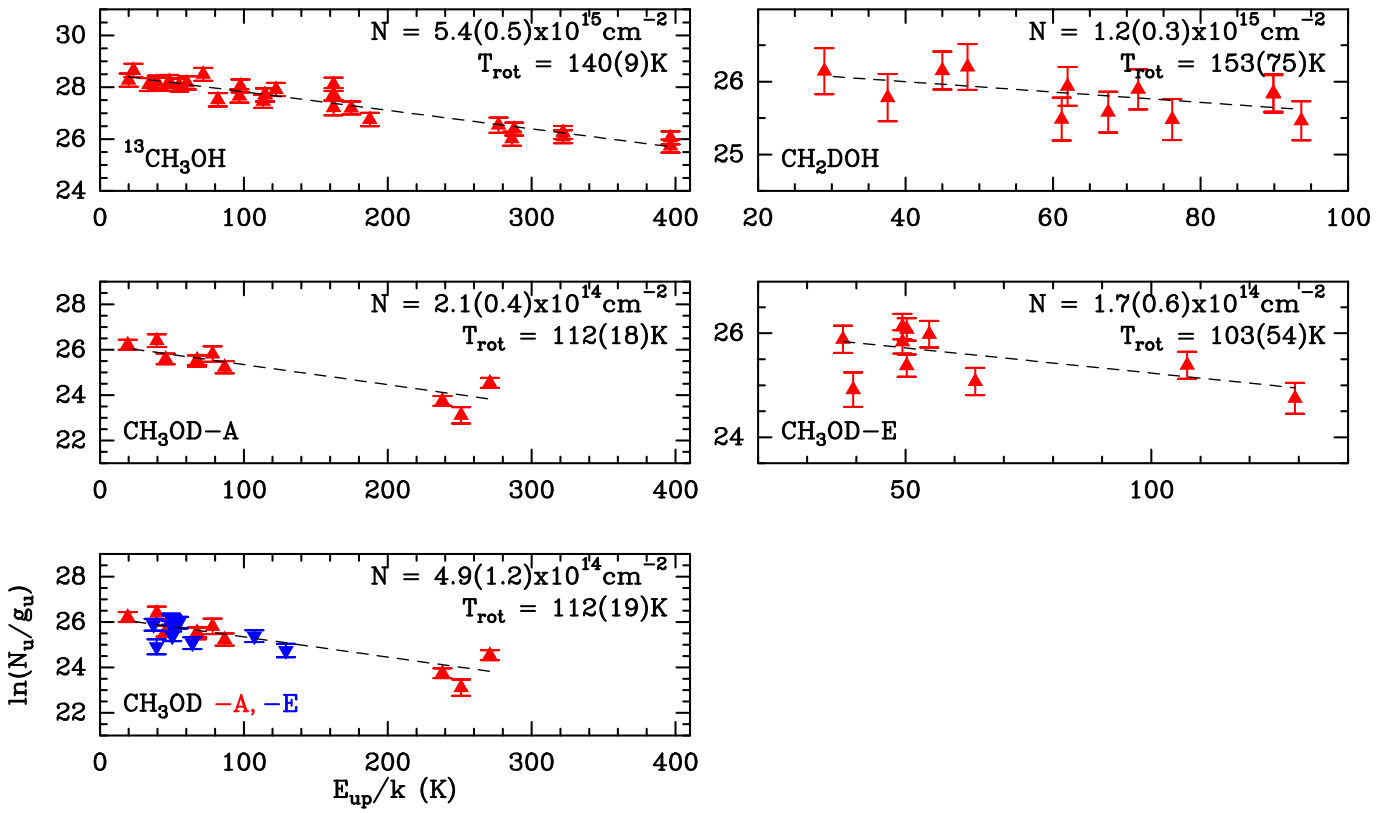

Fig. 2. Population diagram analysis of the ^{13}C-methanol and the deuterated forms. A size of 3.8″ was adopted for the emitting region. In the analysis we separate the methanol E-form from the A-form. However, as shown in the bottom left panel, their respective SLED are consistent with each-other. Finally, please note that the y-range varies from plot to plot.

the following species: $^{13}CH_3OH$, CH_2DOH, CH_3OD (A and E) along with our LTE modelling. In addition, Fig. 1 also displays the spectrum of the $2_{2,0}$-$3_{1,3}$ transition of deuterated water, that is also detected in our survey. Finally, Figures C.1 to C.3 (in Appendix C) display a montage of all the detected transitions associated with the $^{13}CH_3OH$, CH_2DOH, CH_3OD species along with our LTE modeling.

3.2. LTE analysis

The physical properties (excitation temperature, column densities) of the methanol species were obtained from a population diagram analysis of their Spectral Line Energy Distribution (SLED). In the present study, we assume a source size of 3.8″, that corresponds to the ice evaporation region (see Bisschop et al. 2007). The derived column densities are therefore determine and given for a source size 3.8″. We estimate the line opacities, under Local Thermodynamical Equilibrium (LTE) conditions following Goldsmith & Langer (1999, see). We conclude that the $^{13}CH_3OH$, CH_2DOH and CH_3OD emission are optically thin with $\tau \leqslant 0.03$. We note that most of the transitions associated with the main methanol isotopologue are optically thick with $\tau(CH_3OH) \geq 1$. As a consequence, we cannot determine with an accurate enough precision the excitation temperature and the column density of the $^{12}CH_3OH$. We therefore exclude the analysis of the $^{12}CH_3OH$ for the present study.

Figure 2 shows the population diagrams that are all well fitted by a single rotational temperature. More specifically, the population diagram analysis of $^{13}CH_3OH$ yields to $N(^{13}CH_3OH) = (5.4\pm0.5)\times10^{15}$ cm^{-2} and $T_{rot} = 140\pm9$ K. Assuming a $^{12}C/^{13}C$ elemental abundance ratio of 70 for the local ISM (Wilson 1999), we determine the methanol column density $N(CH_3OH) = (3.8 \pm 0.4) \times 10^{17}$ cm^{-2}. Regarding CH_2DOH, we estimate a rotational temperature similar to that of ^{13}C methanol, $T_{rot} = 153 \pm 75$ K, and a column density $N(CH_2DOH)$ of $(1.2 \pm 0.3) \times 10^{15}$ cm^{-2}. For CH_3OD we derive a lower rotational temperature: $T_{rot} = 103 \pm 54$ K (112 ± 18 K) for both the E- and A- forms. Nonetheless, within the error bars, the derived rotational temperatures for the deuterated methanol flavors are in agreement with the one of the^{13}C isotopologue. The derived column densities of both E- and CH_3OD-A are comparable with $N(CH_3OD\text{-E}) = (1.7 \pm 0.6) \times 10^{14}$ cm^{-2} and $N(CH_3OD\text{-A}) = (2.1 \pm 0.4) \times 10^{14}$ cm^{-2}; which results a total CH_3OD column density, $N(CH_3OD), of (3.8 \pm 1.0) \times 10^{14}$ cm^{-2}. We note that the computed total CH_3OD column density is commensurate within the error bars to that found if we treat both substates (E- and A-) simultaneously (see Fig. 2).

Table 1. Physical properties of methanol isotopologues: rotational temperature and column density. A source size of 3.8" was adopted.

Species	T_{rot} (K)	N (10^{14} cm^{-2})
$^{13}CH_3OH$	140 ± 9	54 ± 5
CH_2DOH	153 ± 75	12 ± 3
CH_3OD-E	103 ± 54	1.7 ± 0.6
CH_3OD-A	112 ± 18	2.1 ± 0.4

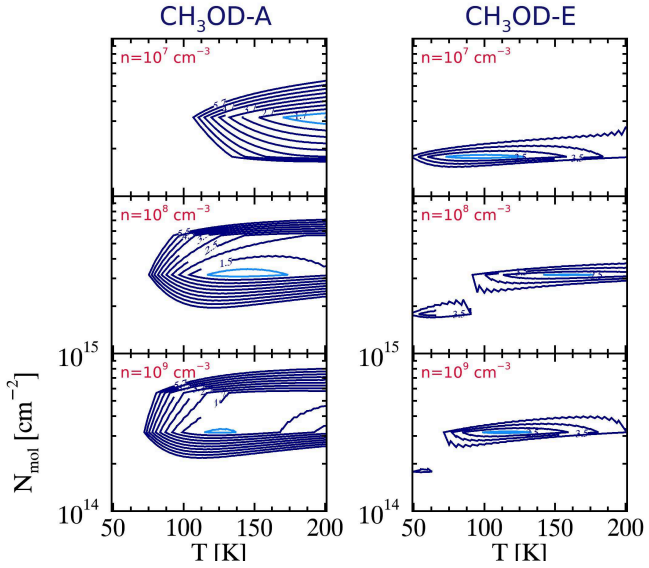

Fig. 3. CH_3OD-A (left column) and CH_3OD-E (right column) χ^2 distributions as computed with RADEX for n=10^7, 10^8 and 10^9 cm^{-3}. The minimum χ^2 is displayed in cyan.

3.3. non-LTE analysis

The present section aims to verify whether the apparent LTE distribution of the CH_3OD targeted transitions is consistent with non-LTE conditions along with the derived densities and temperatures.

For this purpose we have combined the (unpublished) spectroscopic data of CH_3OD (energy levels and radiative rates) with the collisional rate coefficients computed by Rabli & Flower (2010) for the rotational excitation of CH_3OH by H_2. We thus assumed that the -OH H/D substitution has a negligible impact on the scattering dynamics (the change in reduced mass is only 0.2%). The coupled statistical equilibrium-radiative transfer equations were then solved using the RADEX code (van der Tak et al. 2007).

Assuming a source size of 3.8″ and a line-width of 4 km s^{-1}, we ran a grid of models for the following gas densities n=10^7, 10^8 and 10^9 cm^{-3} with the kinetic temperature varying from 20 to 200 K and the CH_3OD column density lying between 1×10^{10} and 1×10^{19} cm^{-2}. Then, we compare the observed and modelled LGV CH_3OD-A and CH_3OD-E integrated fluxes by the mean of the χ^2. The computed results and minimized χ^2 distributions are shown in Figure 3.

There is no common solution for both E- and A-species with a density of 10^7. A common region of minimum χ^2 in the parameter space (N,T) is found for a density in the range 10^8 cm^{-3}-10^9 cm^{-3}. The latter is commensurate with the one derived by Beuther et al. (2012) from PdBI observations as well as that derived by Bisschop et al. (2007) from JCMT observations. Our best fits are obtained for a CH_3OD column density of about $\simeq 3\times10^{14}$ cm^{-2}, a temperature 100–150 K, both consistent with our LTE analysis.

4. Discussion

4.1. D/H in methanol

As can be seen in Table 2, the fractionation degree of singly deuterated methanol is low in NGC 7538-IRS1, with relative abundance values of 0.1% (taking into account the statistical ratio for the -CH_3 functional group). Such values are similar to those reported towards other HMSRs like Orion KL. Thanks to the numerous detected lines for both CH_2DOH and CH_3OD, the relative abundance between the two deuterated flavors is determined with a good accuracy, and is found to equal to 3.2 ±1.5.

Table 2. Deuteration ratios measured towards NGC 7538-IRS1.

Species	Ratios
CH_2DOH/CH_3OH	$(3.2\pm0.8)\times10^{-3}$
CH_3OD/CH_3OH	$(1.0\pm0.4)\times10^{-3}$
CH_2DOH/CH_3OD	3.2 ± 1.5

4.2. Water and HDO

Water does not exhibit the same level of fractionation as methanol in low-mass star-forming regions, with a HDO/H_2O lying in the range 0.01-0.07 (Liu et al. 2011; Parise et al. 2005, 2006; Ratajczak et al. 2011; Coutens et al. 2012; Faure et al. 2015a). However, in Orion-KL water and methanol seem to be fractionated to a similar extent (Neill et al. 2013a). This is likely the result of recent desorption from ice mantles (see further details on thermal H/D exchanges between water and methanol during the warm-up phase in Faure et al. 2015a).

Although only the HDO ($2_{2,0}$-$3_{1,3}$) transition is detected in our data, as shown in Fig. 1, we can roughly estimate the D/H ratio for water combining our result to that of different studies. Indeed, combining the observed HDO integrated flux (~ 0.8±0.1 K km s^{-1}) to the ones measured by Jacq et al. (1990) for the ($3_{1,2}$-$2_{2,1}$) and ($2_{1,1}$-$2_{1,2}$) transitions and, assuming a source size of 3.8″, we derived a HDO column density of about 1.6×10^{15} cm $^{-2}$ and a rotational temperature of ~ 130 K.

From recent Herschel/HIFI observations of water in NGC 7538-IRS1, Herpin et al. (2017) have derived a water abundance, $\chi_{(H_2O)}$, of 8×10^{-6}. Assuming a n_{H_2} of about 10^8 cm^{-3} (see Section 3.3), we estimate a HDO/H_2O ratio lying in the range 10^{-4}-10^{-3} according to the source size taken into account (see also van der Tak et al. 2006).

Incidentally, we note that Herpin et al. (2017) also derived a H_2O abundance of 5×10^{-5} for the very inner part of the hot core, as probed by a THz line observed with SOFIA.

These findings show that the water emission source size gives strong constraints on the deuteration ratio. Therefore, further interferometric observations of water and its isotopologues are clearly needed to investigate in more detail water fractionation in this source.

4.3. Comparison with other sources

We have reported in Fig. 4 the relative CH_2DOH/CH_3OD abundance ratio measured towards a large sample of star forming regions, from low- to high-mass, ordered from left to right by increasing source luminosity. It is immediately apparent that there is a 2 orders of magnitude variation between the sources. More specifically, in low-mass star forming regions, methanol deuteration strongly favors the methyl group (CH_2DOH) by far more than the statistical factor (3), whereas in high-mass the opposite trend is observed.

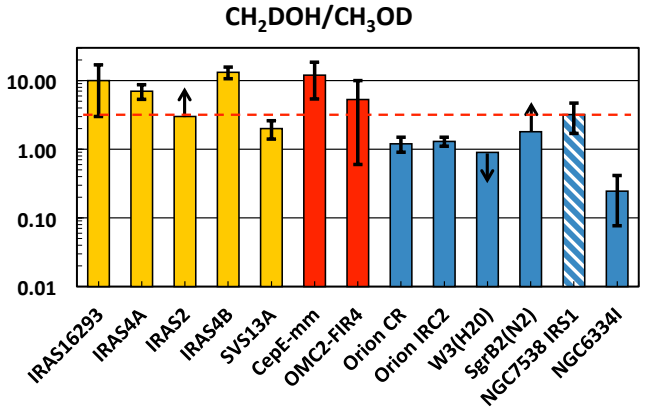

Fig. 4. CH_2DOH/CH_3OD ratios observed towards low (yellow), intermediate (red) and high mass (blue) star forming regions: IRAS16293-2422 (Parise et al. 2002; Jørgensen et al. 2018), IRAS4A, IRAS2, IRAS4B (Parise et al. 2006), SVS13A (Bianchi et al. 2017), CepE-mm (Ratajczak et al. 2011), OMC2-FIR4 (Ratajczak et al. 2011), Orion CR (Neill et al. 2013a), Orion Irc2, W3(H2O), SgrB2(N2) (Belloche et al. 2016), NGC 7538-IRS1 (this work; blue and white stripes) and NGC6334I (Bøgelund et al. 2018). We note that values derived by Parise et al. (2006) and Ratajczak et al. (2011) were divided by a factor of 2 and 1.5, respectively, due to a spectroscopic issue (see Belloche et al. 2016). The dashed red line shows the statistical factor $CH_2DOH/CH_3OD = 3$.

4.4. Modelling

The value of the abundance ratio CH_2DOH/CH_3OD toward NGC 7538-IRS1 is 3.2 ± 1.5, in good agreement with the value of 3 predicted by grain chemistry models (e.g. Charnley et al. 1997; Osamura et al. 2004). In these models, the deuterium fractionation of methanol proceeds in the ice during the early cold prestellar phase through the statistical addition of H and D atoms on CO molecules and the ratio s-CH_2DOH/s-CH_3OD is equal to the statistical value of 3. More recent and sophisticated models also predicts a ratio close to 3 (e.g. Bøgelund et al. 2018). These models however neglect processes occurring in the subsequent warm-up phase. In particular, Faure et al. (2015a) have shown that the s-CH_2DOH/s-CH_3OD ratio can change during this phase as a result of H/D exchanges between the hydroxyl (-OH) functional groups of methanol and water (see details in Faure et al. 2015b). This scenario was successful in explaining both the high value (>3) of the CH_2DOH/CH_3OD abundance ratio towards the low-mass protostar IRAS 16293-2422 and the low-value (<3) measured towards Orion (see Fig. 4).

We have adapted the model of Faure et al. (2015a) to the conditions of NGC 7538-IRS1. First, the density was taken as $n_H = 2 \times 10^8$ cm^{-3} and the (equal) gas and dust temperatures as $T = 100$ K. The methanol abundance (by number) relative to water is 4% (Öberg et al. 2011; Boogert et al. 2015) and the mean water abundance is $5 \times 10^{-5} n_H$. The accreting D/H ratio is inferred from the observed CH_2DOH/CH_3OH ratio (see Table 2) as $\alpha_m = 1.1 \times 10^{-3}$, assuming that the initial (statistical) deuteration of CH_2DOH in the ice is conserved during the hot core phase. The post-evaporative gas-phase chemistry is also entirely neglected (full details can be found in Faure et al. 2015a). The results of the model are plotted in Fig. 5: it is found that the observed CH_2DOH/CH_3OD ratio of 3.2 ± 1.5 can be reproduced for a solid s-HDO/s-H_2O ratio in the range $\sim 8\times10^{-4} - 2\times10^{-3}$. Thus, while the CH_2DOH/CH_3OD ratio of 3.2 ± 1.5 is consistent with a statistical deuteration, the occurence of H/D exchanges cannot be excluded. In particular, it should be noted that H/D exchanges can explain the range of values depicted in Fig. 4, that is CH_2DOH/CH_3OD ratios in the range $\sim 0.1 - 10$. To our knowledge, this is currently the unique mechanism able to explain the non-statistical deuteration of methanol in both low- and high-mass protostars.

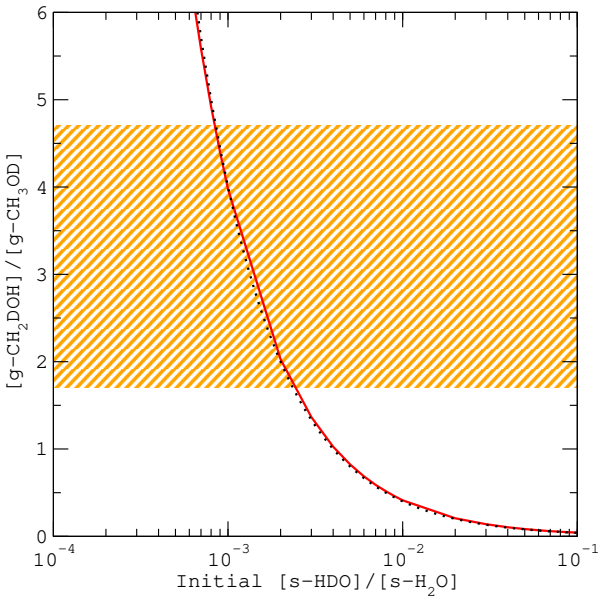

Fig. 5. Gas-phase abundance ratio of the deuterated isotopologues, CH_2DOH/CH_3OD, as function of the initial (cold) water ice deuteration. The dotted line corresponds to the analytic solution CH_2DOH/CH_3OD=0.004/(HDO/H_2O) (see Faure et al. 2015a, for details).The ratio observed toward NGC 7538-IRS1 is represented by the orange hatched zone.

5. Conclusions

To summarize, we have investigated the deuteration of methanol in the high-mass star forming regions NGC 7538-IRS1 using IRAM-30m observations. Our study shows that the fractionation degree of deuterated methanol is low in this source. From the numerous (≥10) detected lines, we estimate a CH_2DOH/CH_3OD relative abundance ratio of 3.2 ± 1.5. Although our findings are commensurate with statistical deuteration at the icy surface of grain mantles, we cannot exclude H/D exchanges between water and methanol at the present time. Further observations of water and HDO are required to address this point.

Acknowledgements. We thank the anonymous referee for his very fruitful comments that have strengthened our paper. This work is supported by the French National Research Agency in the framework of the Investissements d'Avenir program (ANR-15-IDEX-02), through the funding of the "Origin of Life" project of the Univ. Grenoble-Alpes. CF and DF acknowledge support from the Italian Ministry of Education, Universities and Research, project SIR (RBSI14ZRHR). LHX acknowledges financial support from the Natural Sciences and Engineering Research Council of Canada. We also acknowledge the funding from the European Research Council (ERC) under the European Union's Horizon 2020 research and innovation programme, for the Project "The Dawn of Organic Chemistry" (DOC), grant agreement No 741002. This project was carried out under project number 128–12 with the IRAM 30 m telescope. IRAM is supported by INSU/CNRS (France), MPG (Germany), and IGN (Spain).

References

Belloche, A., Müller, H. S. P., Garrod, R. T., & Menten, K. M. 2016, A&A, 587, A91
Beuther, H., Linz, H., & Henning, T. 2012, A&A, 543, A88
Bianchi, E., Codella, C., Ceccarelli, C., et al. 2017, MNRAS, 467, 3011
Bisschop, S. E., Jørgensen, J. K., van Dishoeck, E. F., & de Wachter, E. B. M. 2007, A&A, 465, 913
Bøgelund, E. G., McGuire, B. A., Ligterink, N. F. W., et al. 2018, A&A, 615, A88
Boogert, A. C. A., Gerakines, P. A., & Whittet, D. C. B. 2015, ARA&A, 53, 541
Caselli, P. & Ceccarelli, C. 2012, A&A Rev., 20, 56
Ceccarelli, C., Caselli, P., Bockelée-Morvan, D., et al. 2014, Protostars and Planets VI, 859
Ceccarelli, C., Caselli, P., Herbst, E., Tielens, A. G. G. M., & Caux, E. 2007, Protostars and Planets V, 47
Charnley, S. B., Tielens, A. G. G. M., & Rodgers, S. D. 1997, ApJ, 482, L203
Coutens, A., Vastel, C., Caux, E., et al. 2012, A&A, 539, A132
Faure, A., Faure, M., Theulé, P., Quirico, E., & Schmitt, B. 2015a, A&A, 584, A98
Faure, M., Quirico, E., Faure, A., et al. 2015b, Icarus, 261, 14
Goldsmith, P. F. & Langer, W. D. 1999, ApJ, 517, 209
Herpin, F., Baudry, A., Richards, A. M. S., et al. 2017, A&A, 606, A52
Jacq, T., Walmsley, C. M., Henkel, C., et al. 1990, A&A, 228, 447
Jacq, T., Walmsley, C. M., Mauersberger, R., et al. 1993, A&A, 271, 276
Jørgensen, J. K., Müller, H. S. P., Calcutt, H., et al. 2018, ArXiv e-prints [arXiv:1808.08753]
Lis, D. C., Roueff, E., Gerin, M., et al. 2002, ApJ, 571, L55
Liu, F.-C., Parise, B., Kristensen, L., et al. 2011, A&A, 527, A19
Müller, H. S. P., Menten, K. M., & Mäder, H. 2004, A&A, 428, 1019
Müller, H. S. P., Schlöder, F., Stutzki, J., & Winnewisser, G. 2005, Journal of Molecular Structure, 742, 215
Nandi, A., Qu, C., & Bowman, J. 2018, Journal of computational chemistry
Neill, J. L., Crockett, N. R., Bergin, E. A., Pearson, J. C., & Xu, L.-H. 2013a, ApJ, 777, 85
Neill, J. L., Wang, S., Bergin, E. A., et al. 2013b, ApJ, 770, 142
Öberg, K. I., Boogert, A. C. A., Pontoppidan, K. M., et al. 2011, ApJ, 740, 109
Osamura, Y., Roberts, H., & Herbst, E. 2004, A&A, 421, 1101
Parise, B., Castets, A., Herbst, E., et al. 2004, A&A, 416, 159
Parise, B., Caux, E., Castets, A., et al. 2005, A&A, 431, 547
Parise, B., Ceccarelli, C., Tielens, A. G. G. M., et al. 2006, A&A, 453, 949
Parise, B., Ceccarelli, C., Tielens, A. G. G. M., et al. 2002, A&A, 393, L49
Pearson, J. C., Yu, S., & Drouin, B. J. 2012, Journal of Molecular Spectroscopy, 280, 119
Peng, T.-C., Despois, D., Brouillet, N., Parise, B., & Baudry, A. 2012, A&A, 543, A152
Pickett, H. M., Poynter, I. R. L., Cohen, E. A., et al. 1998, Journal of Quantitative Spectroscopy and Radiative Transfer, 60, 883
Rabli, D. & Flower, D. R. 2010, MNRAS, 406, 95
Ratajczak, A., Taquet, V., Kahane, C., et al. 2011, A&A, 528, L13
Roberts, H., Fuller, G. A., Millar, T. J., Hatchell, J., & Buckle, J. V. 2002, Planet. Space Sci., 50, 1173
van der Tak, F. F. S., Black, J. H., Schöier, F. L., Jansen, D. J., & van Dishoeck, E. F. 2007, A&A, 468, 627
van der Tak, F. F. S., Walmsley, C. M., Herpin, F., & Ceccarelli, C. 2006, A&A, 447, 1011
Walsh, M. S., Xu, L.-H., Lees, R. M., et al. 2000, Journal of Molecular Spectroscopy, 204, 60
Wilson, T. L. 1999, Reports on Progress in Physics, 62, 143
Wirström, E. S., Geppert, W. D., Hjalmarson, Å., et al. 2011, A&A, 533, A24
Xu, L.-H., Fisher, J., Lees, R. M., et al. 2008, Journal of Molecular Spectroscopy, 251, 305
Xu, L. H. & Hougen, J. T. 1995a, Journal of Molecular Spectroscopy, 169, 396
Xu, L. H. & Hougen, J. T. 1995b, Journal of Molecular Spectroscopy, 173, 540
Xu, L.-H., Lees, R. M., Hao, Y., et al. 2014, Journal of Molecular Spectroscopy, 303, 1
Xu, L.-H. & Lovas, F. J. 1997, Journal of Physical and Chemical Reference Data, 26, 17
Xu, L.-H., Walsh, M. S., & Lees, R. M. 1996, Journal of Molecular Spectroscopy, 179, 269

Appendix A: Spectroscopic and Observational line parameters

Tables A.1 to A.4 list the spectroscopic and observational line parameters for the observed CH_3OH-A, CH_3OH-E, $^{13}CH_3OH$, CH_2DOH, CH_3OD-A and CH_3OD-E transitions.

Appendix B: Partition function of CH_3OD

Table B.1 gives the respective CH_3OD-A and CH_3OD-E rotation partition functions we use in the present study.

Appendix C: IRAM-30 m observations overlaid with our LTE modeling for $^{13}CH_3OH$, CH_3OD-A and CH_3OD-E.

Figures C.1 to C.3 show a montage of the detected $^{13}CH_3OH$, CH_2DOH, CH_3OD-A and CH_3OD-E transitions (see Tables A.3 to A.4 for the observational line parameters) along with our LTE modelling.

Table A.1. Methanol

Species	Frequency (MHz)	Quantum numbers	E_{up} (K)	A_{ul} (10^{-5} s^{-1})	Flux (K km s^{-1})	V$_{lsr}$ (km s^{-1})	ΔV (km s^{-1})	T_{peak} (mK)
CH_3OH-E	213159.150	$20_{-4,0} - 19_{-5,0}$	567.0	1.6	1.6 (0.3)	-59.0 (0.0)	4.0 (0.1)	374 (9)
	213377.528	$13_{6,0} - 14_{5,0}$	382.0	1.1	1.4 (0.3)	-59.0 (0.0)	3.5 (0.1)	368 (7)
	213427.061	$1_{1,0} - 0_{0,0}$	15.5	3.4	4.4 (0.9)	-58.8 (0.0)	3.5 (0.0)	1173 (18)
	217886.504	$20_{1,0} - 20_{0,0}$	500.5	3.4	1.8 (0.4)	-59.2 (0.0)	3.7 (0.0)	439 (5)
	218440.063	$4_{2,0} - 3_{1,0}$	37.6	4.7	10.0 (2.0)	-58.1 (0.0)	5.3 (0.1)	1776 (12)
	219983.675	$25_{3,0} - 24_{4,0}$	794.3	2.0	0.4 (0.1)	-59.0 (0.1)	3.1 (0.3)	130 (13)
	219993.658	$23_{5,0} - 22_{6,0}$	768.0	1.7	0.6 (0.1)	-58.9 (0.1)	3.8 (0.2)	143 (8)
	220078.561	$8_{0,0} - 7_{1,0}$	88.7	2.5	2.9 (0.6)	-58.7 (0.0)	4.1 (0.1)	677 (7)
	229589.056	$15_{4,0} - 16_{3,0}$	366.5	2.1	2.2 (0.4)	-59.1 (0.0)	3.1 (0.1)	651 (14)
	229758.756	$8_{-1,0} - 7_{0,0}$	81.2	4.2	5.0 (1.0)	-58.3 (0.0)	4.2 (0.0)	1124 (11)
	230027.047	$3_{-2,0} - 4_{-1,0}$	31.9	1.5	3.0 (0.6)	-58.6 (0.0)	4.2 (0.1)	658 (14)
	230368.763	$22_{4,0} - 21_{5,0}$	674.8	2.1	1.1 (0.2)	-59.0 (0.2)	3.9 (0.5)	274 (62)
	232624.811	$15_{6,1} - 15_{7,1}$	861.9	0.7	0.3 (0.1)	-58.8 (0.1)	3.3 (0.3)	74 (6)
	232645.103	$8_{6,1} - 8_{7,1}$	667.7	0.9	0.4 (0.1)	-58.8 (0.2)	4.1 (0.4)	84 (7)
	232847.103	$9_{6,1} - 9_{7,1}$	688.6	1.0	0.5 (0.1)	-59.0 (0.1)	4.2 (0.3)	106 (6)
	232945.797	$10_{-3,0} - 11_{-2,0}$	182.5	2.1	3.8 (0.8)	-59.0 (0.0)	3.6 (0.1)	999 (15)
	233011.878	$10_{6,1} - 10_{7,1}$	711.7	1.1	0.3 (0.1)	-58.7 (0.2)	3.3 (0.4)	87 (9)
	233121.162	$11_{6,1} - 11_{7,1}$	737.1	1.1	0.5 (0.1)	-59.2 (0.2)	4.2 (0.5)	113 (10)
	233155.874	$12_{6,1} - 12_{7,1}$	764.9	1.0	0.3 (0.1)	-59.0 (0.3)	4.0 (0.8)	68 (10)
	234698.519	$5_{-4,0} - 6_{-3,0}$	114.8	0.6	1.8 (0.4)	-59.0 (0.0)	3.3 (0.0)	527 (6)
	244337.983	$9_{1,1} - 8_{0,1}$	387.7	4.0	1.5 (0.3)	-59.4 (0.1)	4.4 (0.1)	329 (9)
	245094.503	$18_{-6,1} - 17_{-7,1}$	881.0	2.1	0.2 (0.0)	-58.6 (0.2)	3.0 (0.4)	67 (7)
	247161.950	$16_{2,0} - 15_{3,0}$	330.2	2.6	1.9 (0.4)	-59.3 (0.0)	3.5 (0.1)	518 (12)
	247840.050	$12_{-2,1} - 13_{-3,1}$	537.2	6.3	1.7 (0.3)	-58.9 (0.0)	3.7 (0.1)	434 (8)
	247968.119	$23_{1,0} - 23_{0,0}$	653.5	4.4	1.0 (0.2)	-59.0 (0.0)	4.1 (0.1)	228 (5)
	248854.996	$15_{-1,1} - 16_{-2,1}$	683.3	1.3	0.4 (0.1)	-58.7 (0.1)	3.6 (0.2)	107 (5)
	249004.019	$10_{7,1} - 9_{6,1}$	700.5	3.6	0.5 (0.1)	-58.7 (0.1)	3.9 (0.2)	114 (6)
	249192.836	$16_{-3,0} - 15_{-4,0}$	370.4	2.5	1.6 (0.3)	-59.0 (0.0)	4.0 (0.1)	376 (6)
	250970.042	$17_{3,1} - 18_{4,1}$	763.1	7.7	1.0 (0.2)	-59.0 (0.1)	3.7 (0.1)	250 (7)
	254015.377	$2_{0,0} - 1_{-1,0}$	12.2	1.9	3.1 (0.6)	-58.9 (0.3)	4.1 (0.3)	704 (104)
	254419.419	$11_{5,0} - 12_{4,0}$	281.3	1.8	1.8 (0.4)	-58.7 (0.0)	3.2 (0.1)	536 (9)
	259581.398	$24_{1,0} - 24_{0,0}$	709.1	4.9	0.7 (0.1)	-59.0 (0.1)	3.4 (0.2)	191 (8)
	261061.320	$21_{-4,0} - 20_{-5,0}$	615.7	3.0	1.0 (0.2)	-58.8 (0.1)	2.9 (0.3)	327 (29)
	261704.409	$12_{6,0} - 13_{5,0}$	351.9	1.8	1.1 (0.2)	-59.2 (0.1)	3.4 (0.2)	301 (19)
	261805.675	$2_{1,0} - 1_{0,0}$	20.1	5.6	5.3 (1.1)	-58.2 (0.0)	4.4 (0.1)	1132 (15)
	264732.426	$13_{2,1} - 12_{3,1}$	602.6	0.5	0.2 (0.1)	-58.6 (0.2)	3.0 (0.4)	75 (10)
	265289.562	$6_{1,0} - 5_{2,0}$	61.9	2.6	1.5 (0.3)	-59.0 (0.0)	2.9 (0.2)	497 (40)
	266838.148	$5_{2,0} - 4_{1,0}$	49.2	7.7	3.9 (0.8)	-57.9 (0.0)	3.5 (0.1)	1052 (24)
	267887.317	$24_{5,0} - 23_{6,0}$	823.6	3.2	0.5 (0.1)	-59.1 (0.2)	3.5 (0.4)	127 (13)
	268743.954	$9_{-5,0} - 10_{-4,0}$	220.5	1.8	1.8 (0.4)	-59.2 (0.1)	3.8 (0.2)	449 (23)
	271222.675	$26_{3,0} - 25_{4,0}$	854.6	3.8	0.7 (0.1)	-58.7 (0.2)	4.3 (0.4)	154 (11)
	271933.603	$25_{1,0} - 25_{0,0}$	767.0	5.5	0.9 (0.2)	-59.0 (0.1)	3.6 (0.3)	230 (18)
	274022.001	$24_{-7,0} - 25_{-6,0}$	947.6	3.1	0.2 (0.1)	-58.9 (0.2)	3.8 (0.5)	60 (6)

Table A.2. Methanol

Species	Frequency (MHz)	Quantum numbers	E_{up} (K)	A_{ul} (10^{-5} s^{-1})	Flux (K km s^{-1})	V$_{lsr}$ (km s^{-1})	ΔV (km s^{-1})	T_{peak} (mK)
CH_3OH-A	215302.206	$6_{1,+,1} - 7_{2,+,1}$	373.8	4.2	2.4 (0.5)	-59.1 (0.0)	3.6 (0.1)	637 (8)
	217299.205	$6_{1,-,1} - 7_{2,-,1}$	373.9	4.3	1.8 (0.4)	-59.0 (0.0)	3.1 (0.1)	530 (23)
	231281.110	$10_{2,-,0} - 9_{3,-,0}$	165.3	1.8	1.7 (0.3)	-59.0 (0.0)	3.5 (0.1)	460 (18)
	232418.521	$10_{2,+,0} - 9_{3,+,0}$	165.4	1.9	1.6 (0.3)	-58.9 (0.0)	3.0 (0.1)	518 (16)
	232783.446	$18_{3,+,0} - 17_{4,+,0}$	446.5	2.2	2.4 (0.5)	-59.2 (0.0)	3.8 (0.1)	589 (7)
	233795.666	$18_{3,-,0} - 17_{4,-,0}$	446.6	2.2	2.4 (0.5)	-59.2 (0.0)	3.6 (0.0)	617 (7)
	234683.370	$4_{2,-,0} - 5_{1,-,0}$	60.9	1.8	3.7 (0.7)	-58.9 (0.0)	3.6 (0.0)	955 (9)
	243915.788	$5_{1,-,0} - 4_{1,-,0}$	49.7	6.0	6.1 (1.2)	-58.0 (0.0)	4.2 (0.0)	1345 (9)
	246873.301	$19_{3,-,0} - 19_{2,+,0}$	490.7	8.0	1.5 (0.3)	-59.2 (0.0)	3.3 (0.1)	442 (9)
	247228.587	$4_{2,+,0} - 5_{1,+,0}$	60.9	2.2	3.5 (0.7)	-59.0 (0.0)	3.7 (0.1)	876 (14)
	247610.918	$18_{3,-,0} - 18_{2,+,0}$	446.6	8.1	1.5 (0.3)	-59.2 (0.0)	3.3 (0.1)	437 (9)
	248282.424	$17_{3,-,0} - 17_{2,+,0}$	404.8	8.1	1.7 (0.3)	-59.2 (0.0)	3.6 (0.1)	444 (6)
	248885.468	$16_{3,-,0} - 16_{2,+,0}$	365.4	8.2	1.8 (0.4)	-59.2 (0.0)	3.4 (0.1)	482 (9)
	249419.924	$15_{3,-,0} - 15_{2,+,0}$	328.3	8.2	1.8 (0.4)	-59.2 (0.0)	3.5 (0.1)	479 (11)
	249443.301	$7_{4,-,0} - 8_{3,-,0}$	145.3	1.5	1.6 (0.3)	-59.1 (0.0)	4.0 (0.1)	375 (8)
	249451.842	$7_{4,+,0} - 8_{3,+,0}$	145.3	1.5	1.5 (0.3)	-59.1 (0.0)	3.9 (0.1)	372 (8)
	249887.467	$14_{3,-,0} - 14_{2,+,0}$	293.5	8.2	1.5 (0.3)	-59.2 (0.0)	3.1 (0.1)	443 (14)
	250291.181	$13_{3,-,0} - 13_{2,+,0}$	261.0	8.2	2.0 (0.4)	-59.1 (0.0)	3.6 (0.1)	526 (8)
	250506.853	$11_{0,+,0} - 10_{1,+,0}$	153.1	4.2	2.6 (0.5)	-58.6 (0.0)	4.5 (0.1)	535 (7)
	250635.200	$12_{3,-,0} - 12_{2,+,0}$	230.8	8.2	2.3 (0.5)	-59.3 (0.0)	3.7 (0.1)	590 (8)
	250924.398	$11_{3,-,0} - 11_{2,+,0}$	203.0	8.2	2.5 (0.5)	-59.2 (0.0)	3.5 (0.0)	673 (5)
	251164.108	$10_{3,-,0} - 10_{2,+,0}$	177.5	8.2	2.7 (0.5)	-59.1 (0.0)	3.5 (0.1)	711 (12)
	251517.309	$8_{3,-,0} - 8_{2,+,0}$	133.4	7.9	3.1 (0.6)	-59.0 (0.0)	3.5 (0.1)	835 (10)
	251641.787	$7_{3,-,0} - 7_{2,+,0}$	114.8	7.7	3.2 (0.6)	-59.0 (0.0)	3.8 (0.1)	797 (9)
	251738.437	$6_{3,-,0} - 6_{2,+,0}$	98.5	7.4	3.4 (0.7)	-58.8 (0.0)	4.0 (0.0)	800 (8)
	251811.956	$5_{3,-,0} - 5_{2,+,0}$	84.6	7.0	3.6 (0.7)	-58.8 (0.0)	4.3 (0.1)	790 (17)
	251866.524	$4_{3,-,0} - 4_{2,+,0}$	73.0	6.1	3.1 (0.6)	-58.6 (0.0)	4.1 (0.1)	717 (8)
	251890.886	$5_{3,+,0} - 5_{2,-,0}$	84.6	7.0	3.3 (0.7)	-58.5 (0.0)	3.8 (0.1)	818 (8)
	251895.728	$6_{3,+,0} - 6_{2,-,0}$	98.5	7.5	3.4 (0.7)	-58.6 (0.0)	3.8 (0.1)	817 (7)
	251900.452	$4_{3,+,0} - 4_{2,-,0}$	73.0	6.1	3.4 (0.7)	-58.5 (0.0)	4.0 (0.1)	781 (9)
	251905.729	$3_{3,-,0} - 3_{2,+,0}$	63.7	4.4	3.4 (0.7)	-58.7 (0.0)	4.2 (0.1)	629 (8)
	251917.065	$3_{3,+,0} - 3_{2,-,0}$	63.7	4.4	3.0 (0.6)	-58.8 (0.0)	4.1 (0.1)	683 (9)
	251923.701	$7_{3,+,0} - 7_{2,-,0}$	114.8	7.8	3.2 (0.7)	-58.8 (0.0)	3.8 (0.0)	793 (6)
	251984.837	$8_{3,+,0} - 8_{2,-,0}$	133.4	8.0	3.1 (0.6)	-59.0 (0.0)	3.7 (0.1)	780 (10)
	252090.409	$9_{3,+,0} - 9_{2,-,0}$	154.2	8.1	3.2 (0.6)	-59.0 (0.0)	3.7 (0.1)	799 (9)
	252252.849	$10_{3,+,0} - 10_{2,-,0}$	177.5	8.3	2.9 (0.6)	-59.1 (0.0)	3.6 (0.0)	749 (8)
	252485.675	$11_{3,+,0} - 11_{2,-,0}$	203.0	8.4	2.7 (0.5)	-59.1 (0.0)	3.6 (0.0)	708 (8)
	252803.388	$12_{3,+,0} - 12_{2,-,0}$	230.8	8.4	2.5 (0.5)	-59.2 (0.0)	3.5 (0.1)	677 (9)
	253221.376	$13_{3,+,0} - 13_{2,-,0}$	261.0	8.5	2.4 (0.5)	-59.2 (0.0)	3.4 (0.1)	660 (9)
	253755.809	$14_{3,+,0} - 14_{2,-,0}$	293.5	8.6	2.5 (0.5)	-59.2 (0.0)	3.4 (0.1)	694 (11)
	254423.520	$15_{3,+,0} - 15_{2,-,0}$	328.3	8.7	2.6 (0.5)	-59.2 (0.0)	3.7 (0.1)	674 (10)
	255241.888	$16_{3,+,0} - 16_{2,-,0}$	365.4	8.8	2.2 (0.4)	-59.2 (0.0)	3.3 (0.1)	615 (8)
	256228.714	$17_{3,+,0} - 17_{2,-,0}$	404.8	9.0	1.9 (0.4)	-59.3 (0.0)	3.3 (0.1)	545 (10)
	257402.086	$18_{3,+,0} - 18_{2,-,0}$	446.5	9.1	2.8 (0.6)	-59.9 (0.0)	4.3 (0.1)	613 (14)
	258780.248	$19_{3,+,0} - 19_{2,-,0}$	490.6	9.3	2.1 (0.4)	-59.4 (0.0)	3.9 (0.1)	502 (11)
	263793.875	$5_{1,+,1} - 6_{2,+,1}$	360.0	8.2	2.7 (0.5)	-58.5 (0.1)	4.5 (0.1)	566 (13)
	265224.426	$5_{1,-,1} - 6_{2,-,1}$	360.0	8.3	2.2 (0.4)	-59.0 (0.0)	3.6 (0.1)	569 (9)
	267406.071	$17_{1,+,0} - 16_{2,+,0}$	366.3	4.2	5.3 (1.1)	-56.9 (0.1)	7.3 (0.2)	681 (9)
	260381.463	$20_{3,+,0} - 20_{2,-,0}$	536.9	9.4	2.3 (0.5)	-59.8 (0.1)	4.8 (0.1)	438 (11)
	246074.605	$20_{3,-,0} - 20_{2,+,0}$	537.0	8.0	1.7 (0.3)	-59.5 (0.0)	3.7 (0.1)	417 (10)
	229939.095	$19_{5,-,0} - 20_{4,-,0}$	578.6	2.1	1.3 (0.3)	-59.0 (0.1)	3.9 (0.2)	315 (12)
	229864.121	$19_{5,+,0} - 20_{4,+,0}$	578.6	2.1	1.4 (0.3)	-58.8 (0.1)	4.8 (0.2)	281 (9)
	262223.872	$21_{3,+,0} - 21_{2,-,0}$	585.6	9.7	1.3 (0.3)	-59.3 (0.0)	3.5 (0.1)	350 (10)
	245223.019	$21_{3,-,0} - 21_{2,+,0}$	585.7	7.9	1.9 (0.4)	-58.6 (0.2)	4.3 (0.2)	408 (13)
	264325.354	$22_{3,+,0} - 22_{2,-,0}$	636.6	9.9	1.5 (0.3)	-59.3 (0.1)	4.3 (0.2)	325 (14)
	244330.372	$22_{3,-,0} - 22_{2,+,0}$	636.8	7.8	1.5 (0.3)	-59.3 (0.0)	3.9 (0.1)	362 (8)
	271562.485	$17_{2,+,1} - 16_{1,+,1}$	652.6	6.5	1.4 (0.3)	-59.2 (0.1)	4.4 (0.2)	307 (12)
	259273.686	$17_{2,-,1} - 16_{1,-,1}$	652.7	5.6	1.1 (0.2)	-59.0 (0.0)	3.8 (0.1)	270 (6)
	266703.383	$23_{3,+,0} - 23_{2,-,0}$	689.9	10.2	1.0 (0.2)	-59.3 (0.0)	3.2 (0.1)	306 (7)
	266872.190	$14_{6,+,1} - 15_{5,+,1}$	711.0	3.1	0.9 (0.2)	-59.0 (0.1)	3.6 (0.2)	234 (10)
	269374.884	$24_{3,+,0} - 24_{2,-,0}$	745.5	10.5	1.2 (0.3)	-59.2 (0.1)	3.7 (0.3)	310 (21)
	217642.677	$15_{6,-,1} - 16_{5,-,1}$	745.6	1.9	1.1 (0.2)	-58.8 (0.1)	4.4 (0.1)	234 (7)
	272356.098	$25_{3,+,0} - 25_{2,-,0}$	803.4	10.9	1.2 (0.2)	-59.2 (0.0)	3.6 (0.2)	308 (8)
	233916.950	$13_{3,-,2} - 14_{4,-,2}$	868.5	1.4	0.4 (0.1)	-58.7 (0.1)	3.6 (0.2)	115 (4)
	233917.018	$13_{3,+,2} - 14_{4,+,2}$	868.5	1.4	0.4 (0.1)	-58.7 (0.1)	3.5 (0.3)	111 (7)
	268345.816	$20_{4,-,1} - 21_{5,-,1}$	967.6	5.3	0.8 (0.2)	-58.9 (0.1)	4.1 (0.3)	189 (14)
	268346.226	$20_{4,+,1} - 21_{5,+,1}$	967.6	5.3	0.8 (0.2)	-58.5 (0.2)	4.1 (0.4)	189 (14)

Table A.3. ^{13}C Methanol

Species	Frequency (MHz)	Quantum numbers	E_{up} (K)	A_{ul} (10^{-5} s^{-1})	Flux (K km s^{-1})	V$_{lsr}$ (km s^{-1})	ΔV (km s^{-1})	T_{peak} (mK)
$^{13}CH_3OH$	212775.66	$1_{1,0,0} - 0_{0,0,0}$	23.3	3.3	296 (60)	-58.8 (0.1)	2.7 (0.2)	104 (8)
	215707.92	$8_{4,5,-,0} - 9_{3,6,-,0}$	162.3	1.1	134 (33)	-58.7 (0.3)	2.5 (0.7)	51 (12)
	215722.48	$8_{4,4,+,0} - 9_{3,7,+,0}$	162.3	1.1	222 (45)	-58.9 (0.1)	3.3 (0.2)	63 (2)
	216370.39	$10_{2,9,-,0} - 9_{3,6,-,0}$	162.4	1.5	540 (113)	-59.5 (0.2)	4.9 (0.5)	103 (8)
	234011.58	$5_{1,5,+,0} - 4_{1,4,+,0}$	48.3	5.3	1093 (220)	-58.8 (0.0)	3.5 (0.2)	290 (12)
	235881.17	$5_{0,5,0} - 4_{0,4,0}$	47.1	5.6	1044 (209)	-58.8 (0.0)	3.2 (0.1)	307 (7)
	235938.22	$5_{-1,5,0} - 4_{-1,4,0}$	39.6	5.4	1092 (221)	-58.8 (0.1)	3.2 (0.2)	318 (18)
	235960.37	$5_{0,5,+,0} - 4_{0,4,+,0}$	34.0	5.6	1032 (207)	-58.7 (0.0)	3.1 (0.0)	316 (4)
	235971.07	$5_{4,2,-,0} - 4_{4,1,-,0}$	114.8	2.0	498 (103)	-58.6 (0.1)	2.7 (0.3)	176 (19)
	235971.07	$5_{4,1,+,0} - 4_{4,0,+,0}$	114.8	2.0	502 (101)	-58.6 (0.0)	2.7 (0.1)	175 (6)
	235978.62	$5_{-4,2,0} - 4_{-4,1,0}$	122.3	2.0	307 (64)	-58.9 (0.2)	2.6 (0.6)	110 (19)
	235997.23	$5_{3,3,+,0} - 4_{3,2,+,0}$	84.0	3.6	1772 (360)	-57.9 (0.1)	4.6 (0.3)	360 (17)
	235997.23	$5_{3,2,-,0} - 4_{3,1,-,0}$	84.0	3.6	1771 (360)	-57.9 (0.1)	4.6 (0.3)	360 (18)
	236008.39	$5_{2,4,-,0} - 4_{2,3,-,0}$	71.8	4.8	1390 (287)	-57.6 (0.2)	5.1 (0.5)	258 (19)
	236006.10	$5_{3,2,0} - 4_{3,1,0}$	81.9	3.6	1459 (299)	-60.6 (0.2)	5.4 (0.5)	253 (15)
	236016.55	$5_{-3,3,0} - 4_{-3,2,0}$	96.9	3.6	428 (90)	-58.7 (0.1)	2.5 (0.4)	162 (20)
	236041.40	$5_{1,4,0} - 4_{1,3,0}$	55.0	5.5	1002 (202)	-58.7 (0.0)	3.5 (0.1)	267 (8)
	236049.52	$5_{2,3,+,0} - 4_{2,2,+,0}$	71.8	4.8	1300 (260)	-58.5 (0.0)	3.7 (0.1)	332 (5)
	236062.00	$5_{-2,4,0} - 4_{-2,3,0}$	60.0	4.7	1971 (397)	-59.3 (0.1)	4.3 (0.1)	432 (13)
	236062.85	$5_{2,3,0} - 4_{2,2,0}$	56.3	4.7	1973 (397)	-58.2 (0.1)	4.3 (0.2)	431 (18)
	248654.97	$10_{-3,8,0} - 11_{-2,10,0}$	187.5	2.6	234 (48)	-58.4 (0.1)	2.4 (0.2)	91 (7)
	250125.69	$5_{3,2,0} - 6_{2,4,0}$	81.9	1.6	164 (34)	-58.5 (0.1)	2.8 (0.3)	54 (5)
	250784.61	$2_{0,2,0} - 1_{-1,1,0}$	19.9	1.8	179 (37)	-58.7 (0.1)	2.8 (0.3)	61 (6)
	254321.72	$4_{2,2,+,0} - 5_{1,5,+,0}$	60.5	2.3	365 (74)	-58.6 (0.1)	3.1 (0.2)	112 (6)
	254509.36	$10_{3,7,-,0} - 10_{2,8,+,0}$	174.6	8.5	1190 (239)	-58.7 (0.0)	3.3 (0.1)	340 (10)
	254959.40	$7_{3,4,-,0} - 7_{2,5,+,0}$	113.5	8.1	1042 (209)	-58.8 (0.0)	3.1 (0.1)	314 (9)
	255050.97	$6_{3,3,-,0} - 6_{2,4,+,0}$	97.6	7.8	1569 (315)	-58.6 (0.1)	3.9 (0.1)	383 (12)
	251796.08	$17_{3,14,-,0} - 17_{2,15,+,0}$	396.5	8.6	465 (94)	-58.6 (0.1)	3.3 (0.1)	131 (5)
	259036.49	$17_{3,15,+,0} - 17_{2,16,-,0}$	396.5	9.1	667 (135)	-57.8 (0.1)	4.1 (0.2)	152 (6)
	252870.23	$15_{3,12,-,0} - 15_{2,13,+,0}$	321.8	8.7	697 (140)	-58.7 (0.0)	3.4 (0.1)	191 (3)
	257421.79	$15_{3,13,+,0} - 15_{2,14,-,0}$	321.8	9.0	607 (122)	-58.5 (0.0)	3.3 (0.1)	175 (5)
	256826.57	$14_{3,12,+,0} - 14_{2,13,-,0}$	287.8	8.9	758 (153)	-58.7 (0.1)	3.2 (0.2)	221 (9)
	273962.69	$11_{5,7,0} - 12_{4,8,0}$	286.2	2.2	103 (24)	-58.7 (0.2)	1.8 (0.5)	52 (14)
	269530.49	$15_{-1,15,0} - 14_{-2,13,0}$	277.0	3.1	324 (81)	-58.0 (0.3)	2.8 (0.8)	107 (25)

Table A.4. Deuterated Methanol

Species	Frequency (MHz)	Quantum numbers	E_{up} (K)	A_{ul} (10^{-5} s^{-1})	Flux (K km s^{-1})	V$_{lsr}$ (km s^{-1})	ΔV (km s^{-1})	T_{peak} (mK)
CH_2DOH	234471.03	$8_{2,6,0} - 8_{1,7,0}$	93.7	8.4	171 (38)	-57.5 (0.2)	2.8 (0.4)	57 (6)
	255647.82	$3_{2,2,0} - 3_{1,3,0}$	29.0	6.3	101 (28)	-57.9 (0.3)	2.3 (0.8)	41 (11)
	256731.55	$4_{1,4,0} - 3_{0,3,0}$	25.2	6.9	126 (31)	-58.2 (0.3)	3.4 (0.7)	35 (6)
	258337.11	$4_{2,3,0} - 4_{1,4,0}$	37.6	7.0	101 (29)	-58.8 (0.3)	2.9 (0.7)	33 (7)
	264017.72	$6_{1,6,0} - 5_{1,5,0}$	48.4	5.8	182 (51)	-58.2 (0.3)	2.5 (0.6)	68 (14)
	265509.20	$6_{1,6,2} - 5_{1,5,2}$	67.5	7.5	126 (30)	-58.0 (0.2)	2.5 (0.5)	48 (7)
	265682.51	$6_{2,5,0} - 6_{1,6,0}$	61.2	8.2	126 (32)	-58.1 (0.2)	3.0 (0.6)	40 (7)
	267634.61	$6_{0,6,0} - 5_{0,5,0}$	45.0	6.3	187 (40)	-58.2 (0.1)	2.3 (0.2)	77 (6)
	267731.74	$6_{2,5,1} - 5_{2,4,1}$	71.6	7.1	163 (38)	-57.9 (0.1)	2.4 (0.4)	64 (8)
	267741.09	$6_{3,4,1} - 5_{3,3,1}$	89.9	5.9	258 (54)	-58.6 (0.1)	3.2 (0.3)	76 (5)
	267742.05	$6_{3,3,1} - 5_{3,2,1}$	89.9	5.9	261 (55)	-57.5 (0.1)	3.3 (0.3)	76 (5)
	270299.93	$7_{2,6,0} - 7_{1,70}$	76.2	8.8	117(31)	-57.8 (0.1)	2.6 (0.3)	43 (4)
	270734.57	$6_{1,5,1} - 5_{1,4,1}$	62.0	7.8	187 (41)	-58.3 (0.1)	2.5 (0.3)	69 (7)
CH_3OD-E	217132.73	$9_{1,8,0} - 8_{2,6,0}$	107.32	1.7	115 (28)	-58.0 (0.3)	4.2 (0.9)	26 (5)
	245143.16	$5_{-1,5,0} - 4_{0,4,0}$	37.27	5.9	212 (54)	-58.6 (0.3)	3.8 (0.7)	53 (12)
	252624.31	$6_{0,6,0} - 5_{-1,5,0}$	49.39	5.0	207 (47)	-57.6 (0.1)	2.8 (0.3)	70 (10)
	264576.81	$10_{1,9,0} - 9_{2,7,0}$	129.23	3.0	115 (31)	-59.0 (0.3)	3.4 (1.0)	31 (8)
	269844.66	$4_{-2,3,0} - 4_{-1,4,0}$	39.36	11.1	156 (46)	-58.9 (0.3)	1.9 (0.4)	75 (18)
	270581.30	$5_{-2,4,0} - 5_{-1,5,0}$	50.25	11.6	310 (65)	-58.6 (0.1)	3.2 (0.3)	90 (8)
	271079.19	$6_{-1,6,0} - 5_{-1,5,0}$	50.27	7.5	416 (88)	-58.4 (0.1)	3.6 (0.3)	109 (12)
	271417.31	$6_{0,6,0} - 5_{0,5,0}$	49.39	6.1	332 (73)	-57.9 (0.3)	3.9 (0.8)	80 (12)
	272328.66	$6_{2,4,0} - 5_{2,3,0}$	64.21	6.9	187 (48)	-58.3 (0.2)	3.0 (0.5)	58 (13)
	272922.56	$6_{1,5,0} - 5_{1,4,0}$	54.83	7.7	435 (101)	-57.5 (0.3)	3.8 (0.6)	108 (20)
CH_3OD-A	218156.16	$14_{1,13,0} - 14_{0,14,0}$	237.96	9.1	259 (54)	-57.5 (0.4)	3.1 (0.7)	79 (6)
	230105.09	$5_{1,4,0} - 4_{1,3,0}$	39.53	4.4	286 (77)	-58.2 (0.3)	2.8 (0.6)	94 (21)
	232077.53	$15_{1,14,0} - 15_{0,15,0}$	270.96	10.5	740 (150)	-56.9 (0.2)	3.9 (0.4)	180 (8)
	246522.69	$8_{0,8,0} - 7_{1,7,0}$	78.24	8.6	596 (127)	-58.9 (0.7)	6.3 (2.2)	89 (13)
	265235.75	$3_{1,3,0} - 2_{0,2,0}$	19.26	13.2	310 (66)	-58.4 (0.1)	3.1 (0.3)	94 (10)
	271704.94	$6_{0,6,0} - 5_{0,5,0}$	45.67	7.6	244 (72)	-58.8 (0.2)	2.8 (0.4)	81 (24)
	271843.69	$14_{2,12,0} - 14_{1,13,0}$	251	16.5	247 (62)	-58.5 (0.4)	3.4 (0.8)	69 (15)
	272004.50	$6_{2,5,0} - 5_{2,4,0}$	67.49	6.9	295 (67)	-58.1 (0.3)	3.3 (0.7)	83 (13)
	272138.36	$6_{3,3,0} - 5_{3,2,0}$	86.73	6.0	254 (60)	-57.8 (0.3)	3.9 (0.9)	61 (13)
	272417.25	$6_{2,4,0} - 5_{2,3,0}$	67.53	7.0	323 (72)	-58.0 (0.9)	4.6 (0.9)	66 (11)

Table B.1. Rotational partition function for CH_3OD

CH_3OD-A		CH_3OD-E	
T [K]	Q	T [K]	Q
9.375	18.1	9.375	15.5
18.75	52.3	18.75	50.8
37.5	153.5	37.5	153.2
75	458.6	75	458.6
150	1537.5	150	1537.1
225	3319.7	225	3316.7
300	5739.8	300	5727.9

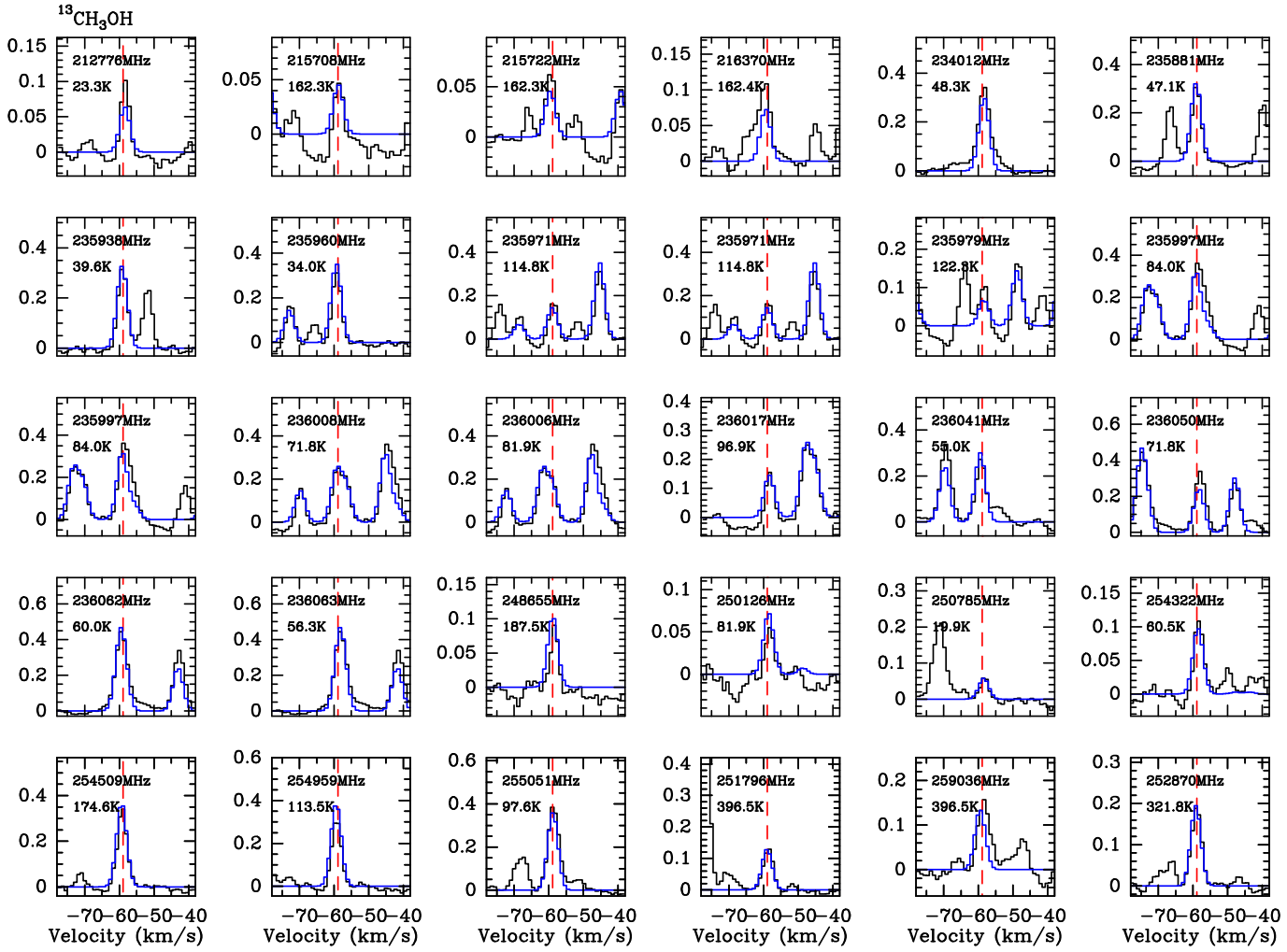

Fig. C.1. Montage of detected transitions associated with the methanol ^{13}C isotopologue towards NGC 7538-IRS1. Our LTE modelling is displayed in blue. Intensities are expressed in unit of T_{mb}. The red dashed line marks the ambient cloud velocity $v_{LSR} = -58.9$ km s^{-1}.

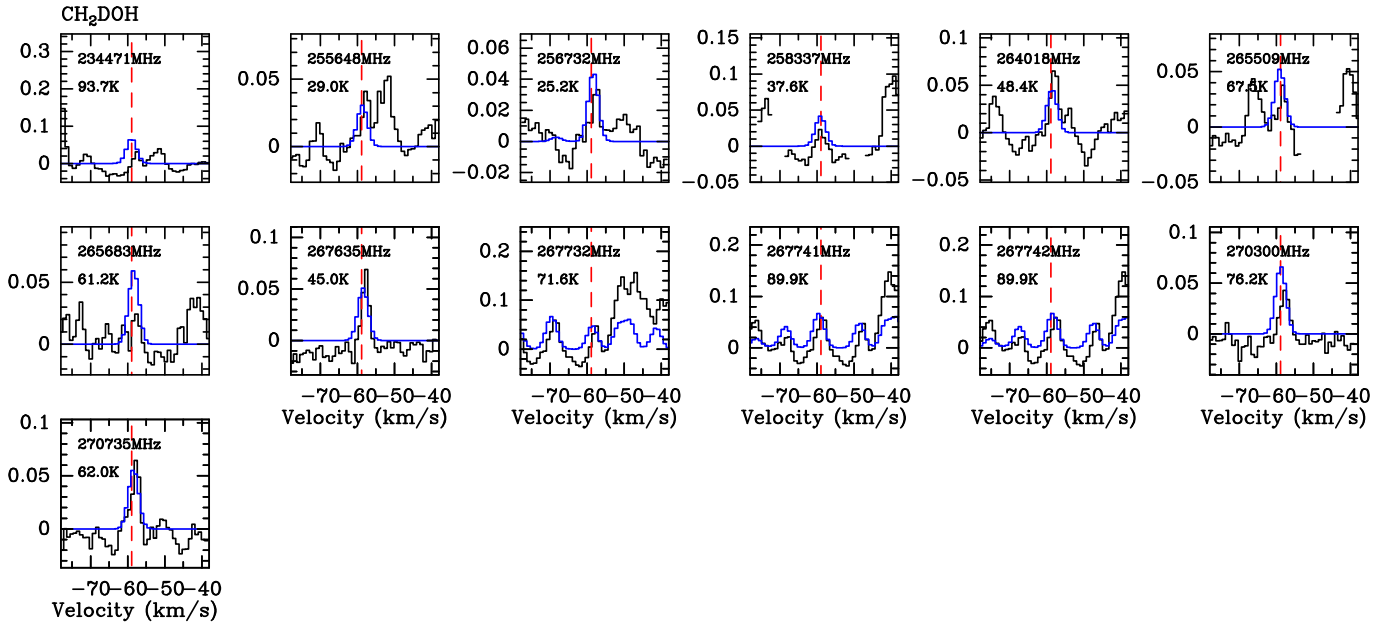

Fig. C.2. Montage of detected transitions associated with the deuterated CH_2DOH methanol towards NGC 7538-IRS1. Our LTE modelling is displayed in blue. Intensities are expressed in unit of T_{mb}. The red dashed line marks the ambient cloud velocity $v_{LSR} = -58.9$ km s^{-1}.

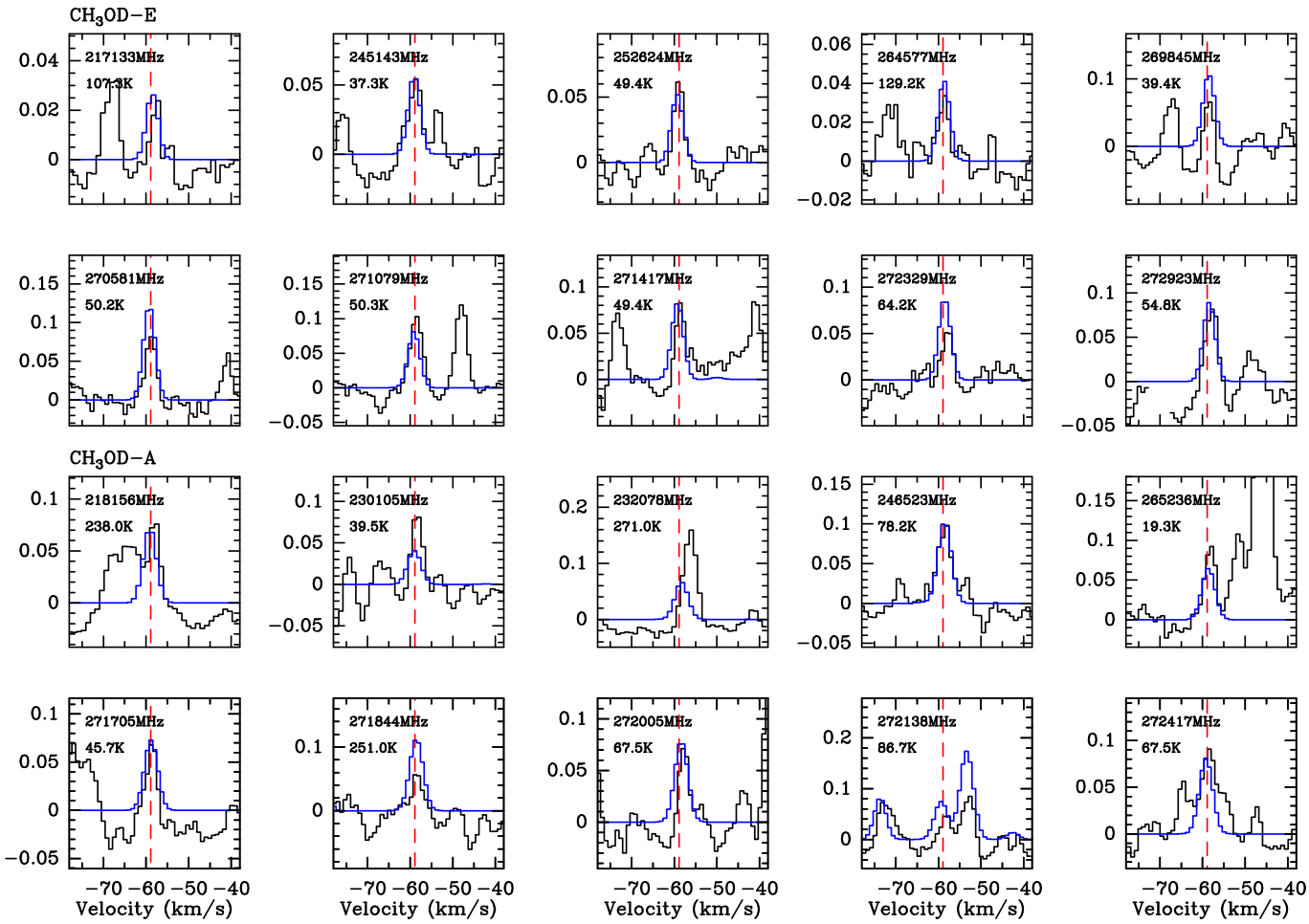

Fig. C.3. Montage of detected transitions associated with the CH_3OD, -A and -E forms towards NGC 7538-IRS1. Our LTE modelling is displayed in blue. Intensities are expressed in unit of T_{mb}. The red dashed line marks the ambient cloud velocity $v_{LSR} = -58.9$ km s^{-1}.